Surface Reconditioning of Lithium Metal Electrodes by Laser Treatment for the Industrial Production of Enhanced Lithium Metal Batteries

Johannes Kriegler,* Heiko Ballmes, Serge Dib, Ali Gökhan Demir, Lucas Hille, Yunhao Liang, Lovis Wach, Steffen Weinmann, Josef Keilhofer, Kun Joong Kim, Jennifer L. M. Rupp, and Michael F. Zaeh

Incorporating lithium metal anodes in next-generation batteries promises enhanced energy densities. However, lithium's reactivity results in the formation of a native surface film, affecting battery performance. Therefore, precisely controlling the chemical and morphological surface condition of lithium metal anodes is imperative for producing high-performance lithium metal batteries. This study demonstrates the efficacy of laser treatment for removing superficial contaminants from lithium metal substrates. To this end, picosecond-pulsed laser radiation is proposed for modifying the surface of lithium metal substrates. Scanning electron microscopy (SEM) revealed that different laser process regimes can be exploited to achieve a wide spectrum of surface morphologies. Energy-dispersive X-ray spectroscopy (EDX) confirmed substantial reductions of ≈80% in oxidic and carbonaceous surface species. The contamination layer removal translated into interfacial resistance reductions of 35% and 44% when testing laser-cleaned lithium metal anodes in symmetric all-solid-state batteries (ASSBs) with lithium phosphorus sulfur chloride (LPSCl) and lithium lanthanum zirconium oxide (LLZO) solid electrolytes, respectively. Finally, a framework for integrating laser cleaning into industrial battery production is suggested, evidencing the industrial feasibility of the approach. In summary, this work advances the understanding of lithium metal surface treatments and serves as proof of principle for its industrial applicability.

1. Introduction

Lithium-ion batteries (LIBs) have become an indispensable cornerstone of modern society, serving as electrochemical energy storage devices that power manifold technologies, most notably electric vehicles.[1] Three decades of continuous technological improvements by materials research and engineering[2] have advanced LIBs with conventional intercalation electrodes toward their material-related electrochemical energy limits.[3,4] The strive for higher specific energies and volumetric energy densities reasons the present intensive research in next-generation lithium metal battery technologies,[5–7] including all-solid-state batteries (ASSBs),[4,8,9] lithium-sulfur batteries,[10] and lithium-air batteries.[11] Lithium metal, with its low electrochemical potential of −3.04 V versus the standard hydrogen electrode and high theoretical specific capacity of ≈3860 mAh g^{-1}, is widely regarded as the most auspicious anode material.[12]

Despite these benefits and the long-year application of lithium metal anodes in

J. Kriegler, L. Hille, Y. Liang, L. Wach, J. Keilhofer, M. F. Zaeh
Technical University of Munich; TUM School of Engineering and Design
Department of Mechanical Engineering
Institute for Machine Tools and Industrial Management
Boltzmannstr. 15, 85748 Garching, Germany
E-mail: johannes.kriegler@iwb.tum.de

H. Ballmes
Schaeffler Technologies AG & Co. KG
91074 Herzogenaurach, Germany

S. Dib, A. G. Demir
Department of Mechanical Engineering
Politecnico di Milano
Via La Masa 1, Milan 20158, Italy

S. Weinmann, K. J. Kim, J. L. M. Rupp
TUM School of Natural Sciences
Department of Chemistry
Technical University of Munich
85747 Garching, Germany

J. L. M. Rupp
TUMint. Energy Research GmbH
Lichtenbergstr. 4, 85748 Garching, Germany

**ADVANCED
SCIENCE NEWS**

www.advancedsciencenews.com

**ADVANCED
FUNCTIONAL
MATERIALS**

www.afm-journal.de

primary batteries,[2] several fundamental electrochemical issues hinder the commercial success of rechargeable lithium metal secondary batteries. The persisting unsolved hurdles involve the safety-critical formation of needle-like lithium dendrites resulting from inhomogeneous lithium plating/stripping,[13,14] large volume changes during the charging/discharging,[5] and the low interface stability due to high reactivity.[15] Among the consequences are escalating impedances and low coulombic efficiencies, curtailing battery lifetime.[16,17]

Utilizing lithium metal anodes in advanced batteries demands knowledge and precise control of the chemical and morphological surface conditions prior to integration. Typically, battery-grade lithium metal is extracted from molten lithium chloride via electrolysis[18] and subsequently shaped into foil substrates via extrusion and rolling processes.[19,20] Moreover, vapor-based[21,22] or liquid-based[23] techniques are researched for manufacturing micrometer-thick lithium coatings.

Pure lithium metal reacts with atmospheric constituents, such as nitrogen, oxygen, water, and carbon dioxide,[24] forming an inorganic native passivation layer. The resulting surface layer consists of various chemical compounds, including lithium carbonate (Li_2CO_3), lithium hydroxide (LiOH), lithium oxide (Li_2O),[25] lithium nitride (Li_3N), lithium carbide (Li_2C_2),[26] and lithium oxalate ($Li_2C_2O_4$).[27] It is generally accepted that such passivation films comprise a bilayer structure consisting of an outer layer of Li_2CO_3, $Li_2C_2O_4$, and LiOH phases and an inner Li_2O layer, transitioning to the pure lithium metal bulk.[25,27–30] The outer layer is typically thinner, with thicknesses of up to 20 nm, while the inner layer can extend to 100 nm.[30,31] The exact passivation layer composition fluctuates based on the environmental conditions during production, transit, storage, and processing.[32]

The passivation layer is pivotal as it affects the thermodynamics and kinetics of reduction processes at the lithium–electrolyte interface,[33] contributing to non-uniform ionic surface conductivities and promoting lithium dendrite growth.[14,34] To counteract degradation, lithium metal substrates undergo pre-passivation before shipping to end-users,[35] e.g., by carbon dioxide (CO_2) gas treatment,[36] phosphorous coating,[37] or fluorination.[30] Nonetheless, the specific surface composition and morphology of lithium metal substrates usually remain unknown, complicating their incorporation into batteries and often requiring additional expensive surface treatments.
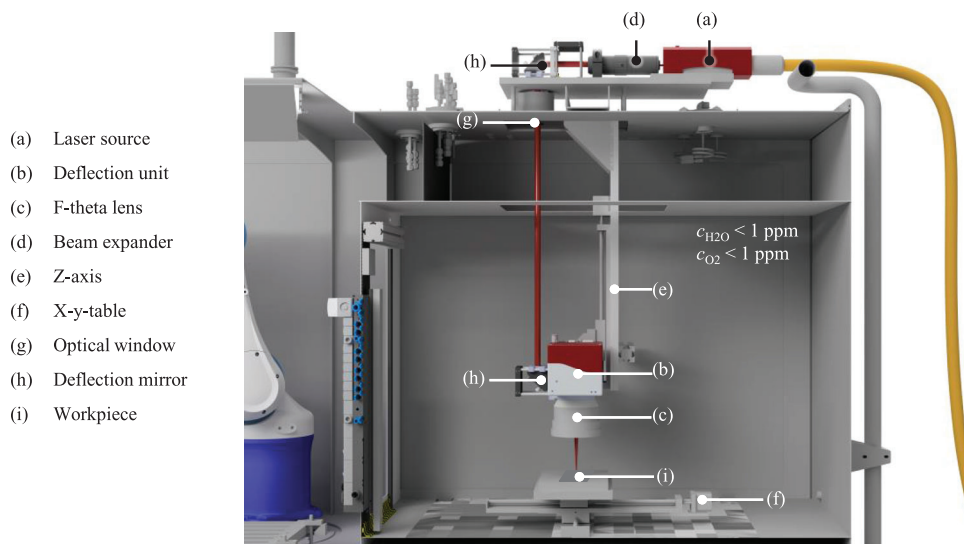
In laboratory settings, surface contaminants are often removed by manual techniques,[26] such as scraping with a scalpel,[38] polishing with abrasive paper[39] or a toothbrush,[40] and adhesive tape stripping.[39] Clearly, these methods suffer from limited reproducibility and scalability, especially for delicate and thin lithium metal foils. Thus, calendering[41] and abrasive sandblasting[42] have been proposed as more industrially feasible alternatives for diminishing the native surface layer. Post-cleaning, an artificial solid electrolyte interphase (SEI) may be superimposed on the high-purity lithium surface to enhance the electrochemical stability and interface contact, thereby improving the electrochemical performance in combination with liquid and solid electrolytes.[43,44,9] However, the final surface condition depends on the constitution of the original surface film,[30,33] necessitating precise control over reaction conditions and contamination levels.[5]

Not only the chemical composition but also the surface morphology plays a crucial role in lithium metal's electrochemical plating and stripping.[45] Strategies to magnify the active surface area for decreasing the effective areal current densities and, thus, mitigating the risk of lithium dendrite growth include surface pattering by micro-needles,[46,47] molds,[48] or abrasive sandblasting.[42] Besides, lithium powder electrodes are tested, inherently offering higher surface areas than standard lithium metal foils.[49,50] Other research concentrates on eliminating surface imperfections, such as cracks or stress lines, that could trigger irregular lithium deposition, referred to as high surface area lithium.[39,51,52] Reducing surface roughness and eliminating surface defects on lithium metal substrates[41] homogenizes the initial current density distribution, diminishing the likelihood of early dendrite formation.[39] Several techniques were proposed to create flat and smooth lithium metal substrates, including calendering,[41] electrochemical[53] or mechanical polishing,[39] and pulsed laser deposition.

The promise of improved lithium metal batteries encourages the search for reproducible methods to adjust the surface chemistry and morphology of lithium metal substrates.[45] Various laser micro-processing techniques operating in partly overlapping process regimes are established for a broad spectrum of technical applications and present promising options for improving product functionality by precisely tuning surface quality and texture.

First, laser micro-structuring by selective material ablation generates deterministic surface structures. In the battery field, this technique has found utility in increasing the anode–electrolyte[54,55] and cathode–electrolyte contact area[56–58] as well as in inserting directed pores for tortuosity reduction.[59–61] Second, laser micro-polishing is applied to smooth surface roughness by combining remelting and ablation.[62–68] Third, laser micro-cleaning focuses on removing top-layer surface contaminants through targeted material removal.[69–74] In the context of battery research, laser radiation was successfully used for removing Li_2CO_3 from the surface of lithium garnet-type ceramic electrolytes[75] and nickel-rich cathode active materials.[76] Besides, laser cleaning was applied to remove excessive binders from the surfaces of LIB cathodes.[77]

In this work, a pioneering, scalable approach utilizing picosecond laser pulses for reconditioning the surface of lithium metal foil substrates is introduced. The influence of various laser process parameters on the resulting surface microstructure is comprehensively investigated. Elemental analyses indicate that oxygen and carbon species on the lithium metal surface can be significantly reduced, enhancing the surface quality of lithium metal electrodes. Moreover, an electrochemical proof of principle is provided by discussing the electrochemical performance of laser-treated lithium metal anodes incorporated into symmetrical ASSBs based on lithium lanthanum zirconium oxide (LLZO)[78–81] and lithium phosphorus sulfur chloride (LPSCl)[82–84] as exemplary garnet oxide and argyrodite sulfide solid electrolytes, respectively. Both materials are among the most promising candidates for practical ASSBs.[85,86,9] Finally, a framework for integrating the developed process into high-throughput industrial battery production lines is recommended, and processing rates are estimated. The suggested technique for efficiently removing passivation

ADVANCED
SCIENCE NEWS
www.advancedsciencenews.com

ADVANCED
FUNCTIONAL
MATERIALS
www.afm-journal.de

Figure 1. A computer aided design rendering of the laser system incorporated in a micro environment is displayed. A red line indicates the laser beam path. After emission from the laser source, the laser beam is guided through a beam expander to extend the raw beam diameter and vertically deflected by a mirror to introduce it into the glovebox through an optical window. Subsequently, a second deflection mirror directs the laser beam into the deflection unit, which controls the laser beam trajectory on the workpiece. The laser beam is focused by an F-theta lens mounted on the deflection unit.

layers serves as procedural enhancement in industrial lithium foil manufacturing, facilitating the management of interfacial resistances and interphase formation in lithium-based batteries with liquid[30,33] and solid electrolytes.[32] Moreover, super-clean lithium metal anodes might facilitate lithiation during direct contact pre-lithiation,[13,87] an advanced manufacturing method for prolonging the lifetime of LIBs with conventional carbonaceous or silicon-based anodes.

Laser treatment presents several distinct advantages relative to traditional lithium metal surface cleaning methods, such as mechanical scraping. First, virtually arbitrarily thin substrates can be processed without physical damage due to the non-contact working principle. Second, the fine adjustability of the process parameters allows for the reproducible generation of diverse surface structures, concurrently limiting unnecessary material removal. Third, the scalability of the process makes it suitable for roll-to-roll processing, indicative of its adaptability to mass production environments. Fourth, the laser-based approach stands out as both economically attractive and environmentally sustainable because of the low energy consumption, avoidance of polishing agents, and omission of mechanical tool wear.

Collectively, this research provides scientific insights into the mechanisms by which laser radiation can be employed in an industrial setting to eliminate surface contaminations from lithium metal foil substrates, a pivotal step toward the fabrication of enhanced lithium metal batteries.

2. Experimental Section

2.1. Lithium Metal Substrate

Commercial battery-grade lithium metal foil substrates (China Energy Lithium, China) composed of a 10-μm-thick copper current collector and a 20-μm-thick pure lithium metal coating were used for the experiments. The substrates were received from the supplier as roll good in an air-tight pouch bag containing an argon atmosphere. The pouch bag was opened and stored in a glovebox incorporating argon atmosphere ($c_{H2O} < 1.0$ ppm and $c_{O2} < 1.0$ ppm) from delivery until the conduction of the experiments. In order to assure comparability, all materials used in the conducted experiments stemmed from the same material batch.

2.2. Laser System

The laser-based surface conditioning was performed using a laser system incorporated in an argon-filled glovebox (**Figure 1**). The residual atmospheric fractions of H_2O and O_2 were monitored with adequate sensors and were kept below 1.0 ppm by a gas purification unit throughout the experiments. An additional purification unit limited the amount of nitrogen within the experimental environment, restricting the formation of Li_3N.[32]

The employed pulsed ytterbium fiber laser (YLPP-25-3-50-R, IPG Photonics, USA) provides peak pulse energies of 25 μJ at pulse repetition rates up to 1883 kHz, resulting in a maximum average power of ≈47 W. Laser pulses with a duration of 2 ± 1 ps were emitted at a fixed infrared wavelength of 1030 nm. The laser beam source was located outside the glovebox system, and the laser beam was guided into the box and in the scanning optics as a free beam passing a fused-silica beam expander (Variable Beam Expander, Edmund Optics GmbH, Germany) and several mirrors. A high-speed 2D-scanning optic (Superscan IV, Raylase, Germany) with a maximum angular velocity ω of up to 200 rad s^{-1} deflected the laser beam.

An F-theta lens (JENarTM SilverlineTM, Jenoptics, Germany) with a focal length f of 160 mm complemented the optical set-up, resulting in a scan field of ≈78 × 78 mm^2, a focal radius of $w_0 = 17.5$ μm, and a Rayleigh length $z = 644$ μm. The latter two parameters were determined using a caustic measurement instrument and fitting functions according to ISO 11146-1, aligning well with theoretical calculations.

Table 1. Parameter levels for the full factorial experimental laser process study based on an infrared picosecond-pulsed laser arrangement directed to the lithium surfaces. The peak pulse fluence F_0 and the line overlap γ result from the pulse energy E_p and the hatch distance d_h, respectively.

Parameter	Levels
Pulse repetition rate f/kHz	50, 1003
Pulse energy E_p/µJ	1.25, 3.75, 6.25, 8.75, 11.25, 13.75, 16.25, 18.75, 21.25
Pulse overlap PO/%	50, 60, 70, 80, 90
Hatch distance d_h/µm	10, 20
Peak pulse fluence F_0/J•cm^{-2}	0.26, 0.78, 1.30, 1.82, 2.34, 2.86, 3.38, 3.90, 4.42
Line overlap γ/%	42.9, 71.4

2.3. Laser Processing Experimental Design

Single and multi-pulse ablation thresholds, i.e., threshold fluences F_{th}, of lithium metal were determined following a well-known method to diagnose the energy distribution of Gaussian laser beams by Liu.[88] Therefore, drillings were manufactured by single pulses as well as trains of 10, 100, and 1000 pulses at a pulse repetition rate f of 50 kHz. Average diameters D of three drillings each measured in two perpendicular directions were calculated and ablation thresholds F_{th} were obtained by fitting according to

$$D^2 = 2w_0^2 \cdot \ln\left(\frac{F_0}{F_{th}}\right) \tag{1}$$

using the peak pulse fluences F_0 and the laser beam focal radius w_0.[88]

Thereby, the peak pulse fluence F_0 was calculated from the pulse energy and the focal radius according to

$$F_0 = \frac{2 \cdot E_p}{\pi \cdot w_0^2} \tag{2}$$

A full-factorial experimental plan was established to assess the influence of the pulse energy E_p, the pulse repetition rate f, the pulse overlap PO (introduced in the following Equation (4)), and the hatch distance d_h (Table 1). The average laser power P is obtained by
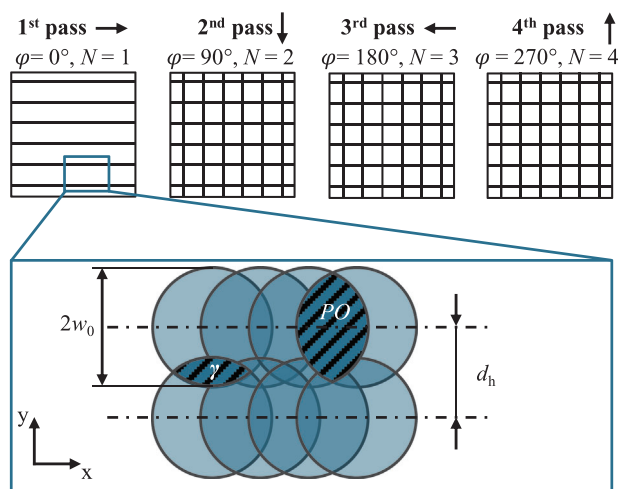
$$P = E_p \cdot f \tag{3}$$

The pulse overlap PO results from the scanning speed v, the pulse repetition rate f and the laser beam's focal radius w_0 according to

$$PO = \left(1 - \frac{v}{2 \cdot f \cdot w_0}\right) \tag{4}$$

Analogously, the line overlap γ can be calculated from the hatch distance d_h by

$$\gamma = \left(1 - \frac{d_h}{2 \cdot w_0}\right) \tag{5}$$

Figure 2. The schematic shows the tested single-pass and multi-pass scanning strategies. The laser parameters later used in this study for lithium metal surface modification were calibrated through the evaluation of the resulting surface morphology.

The laser process study comprised 180 parameter sets, which were tested in a single-pass scanning strategy (**Figure 2**). A delay time of 5 ms was set between every scan line to avoid heat accumulation in the workpiece. Moreover, multi-pass scanning strategies were tested, encompassing up to four passes N at alternating perpendicular scan angles φ. After laser treatment, the samples were subjected to analyses without any other post processing.

2.4. Optical Analyses

The lithium metal surface morphology was analyzed before and after laser treatment using a scanning electron microscope (SEM) (JSM-IT200, Jeol, Germany).

Topography images were recorded using a laser scanning microscope (VK-X 1000, Keyence, Japan). The surface roughness of lithium metal foil samples, both before and after laser cleaning was quantified using the area-based arithmetical mean height Sa, following the guidelines outlined in DIN ISO 25 178.[89]

Additionally, elemental analyses were performed with the associated energy-dispersive X-ray spectroscopy (EDX) module. The average emission generation depth of EDX depends on the electron acceleration voltage and is in the range of the surface passivation layer thickness.[28] Thus, the acceleration voltage was set to a low value of 1 kV to measure the atomic fractions within a shallow penetration depth.[28] Moreover, count maps were recorded, cumulating 90 frames at acceleration voltages of 1 – 5 kV to vary the intrusion depth.[28] The field of view was shifted for every count map to avoid alterations on the lithium metal substrate surface by exposure to the electron beam.[28] The samples were transported from the glovebox to the SEM in air-tight containers to avoid contact of the lithium metal with the ambient atmosphere. The SEM was located in a dry room with a dew point of less than −45 °C and the specimens were subjected to dry room conditions for less than 5 min before analysis.

2.5. Solid Electrolyte Fabrication

Cubic-phase $Li_{6.45}Al_{0.05}La_3Zr_{1.6}Ta_{0.4}O_{12}$ (LLZO) powders were synthesized via a solid-state reaction at a batch size of 100 g. Precursor powders with stoichiometric amounts of anhydrous lithium hydroxide (99.995%), lanthanum (III) hydroxide (99.95%), zirconium (IV) oxide (99.7%), aluminum oxide (99%), and tantalum (V) oxide (99.85%) were prepared with an excess of 15 wt.% LiOH (all constituents from Thermo Scientific, Germany). The powders were then homogeneously mixed in a zirconia (ZrO_2) jar with ZrO_2 milling beads (Retsch, Germany) and absolute ethanol using planetary ball milling (PM100, Retsch, Germany). The powders were dried and uniaxially pressed into pellets at 0.5 MPa before calcination in ambient air at 750 °C for 2 h. After calcination, the green bodies were pre-sintered for an isothermal hold at 1050 °C for 5 h to stabilize the cubic phase. Subsequently, the pellets were ground in a mortar and ball milled for 8 h each at 175 rpm. After drying, the powders were sieved for 30 min in a 43 µm mesh to assure monodisperse particle distributions (d50 = 0.5 µm, d90 = 1 µm) and annealed at 700 °C for 5 h to remove Li_2CO_3 impurities. Powders were then stored in an argon-filled glovebox (c_{H2O} < 0.1 ppm, c_{O2} < 0.1 ppm). Sintered pellets were fabricated by uniaxially pressing the pre-synthesized powders at 5 MPa with a 13 mm die and isothermal sintering the green pellets at 1050 °C for 5 h under oxygen flow in magnesium oxide (MgO) crucibles (heating rate of 5 °C min^{-1}). Dense pellets of ≈11 mm in diameter and a density of ≈95% resulted. After sintering, LLZO pellets were dry polished using silicon carbide paper with grid sizes of 500, 800, 1200, 2400, and 4000 to a thickness of 700 µm. The pellets were annealed in an argon-filled glovebox at 600 °C for 2 h to remove Li_2CO_3 impurities on the surface.

Moreover, argyrodite-type solid electrolyte separators were prepared by coating a Li_6PS_5Cl (LPSCl) (POSCO JK Solid Solution Co. Ltd, Korea) binder slurry on Mylar foil (PPI Adhesive Products, Ireland) under an inert atmosphere (c_{H2O} < 1.0 ppm, c_{O2} < 1.0 ppm) using an automated doctor blade with a coating gap of 150 µm. After drying at ambient conditions, the samples were uniaxially compressed with a pressure of 270 MPa, resulting in typical thicknesses and porosities of ≈30 µm and ≈10 vol.%, respectively. Solid electrolyte separators with a diameter of 15 mm were stamped out.

2.6. Coin Cell Fabrication

Lithium metal surface areas of 20 × 20 mm^2 were laser-treated using a reference parameter set (F_0 = 1.82 J cm^{-2}, f = 50 kHz, PO = 60%, d_h = 10 µm) characterized in chapter 3 of this work. Subsequently, electrodes were laser-cut (v = 0.3 m s^{-1}, E_p = 21.25 µJ, and f = 1833 kHz) from lithium metal substrates in a pristine state and substrates that had undergone laser treatment with a reference parameter set.

Symmetric all-solid-state lithium metal batteries and liquid electrolyte lithium metal batteries were manufactured to test the electrochemical performance of laser-cleaned lithium metal electrodes. The 2032-type coin cells were manually assembled in a glovebox (GS MEGA E-LINE, GS Glovebox, Germany) under an argon atmosphere (c_{H2O} < 1.0 ppm, c_{O2} < 1.0 ppm). Separators, spacers, springs, and housing components were dried in an oven (B-585, Büchi, Switzerland) at 80 °C for 12 h. The total thickness of the spacers amounted to 1.5 mm and the internal cell pressure was set by a spring to 0.2 ± 0.01 MPa.

A complete electrode overlap was ensured by electrode diameters of 6/8 and 9/11 mm for the LLZO and LPSCl ASSBs, respectively. Layer annealing by heating or pressurization was omitted to prevent any potential alterations to the sample surfaces.

For the liquid electrolyte lithium metal batteries, electrodes with a diameter of 12 mm were utilized. Two layers of glass fiber separator (Type 691, VWR, USA) with a diameter of 16 mm were placed between the electrodes. For the cells with laser cleaned lithium metal anodes, the laser-cleaned surfaces were in contact with the separators, facing each other. Hundred microliters of liquid electrolyte (LP572, BASF, Germany) containing 1 mol lithium hexafluorophosphate ($LiPF_6$) conducting salt dissolved in ethylene carbonate and ethyl methyl carbonate solvent with a mass fraction of 3:7 and 2 wt.% vinylene carbonate was added using a pipet before closing the cell by mechanical crimping.

2.7. Electrochemical Characterization

The electrochemical evaluation of symmetric coin cells was conducted inside a controlled climate chamber (ED-115, Binder, Germany) at a constant temperature of 25 °C using a potentiostat (VSP-3e, Bio-Logic, France) with the corresponding software EC-Lab.

For the analysis of the ASSBs, galvanostatic electrochemical impedance spectroscopy (EIS) was employed. Measurement points were recorded across a frequency spectrum ranging from 1 MHz to 100 mHz at an amplitude of 10 mV, and averaged over three measurements. The impedance data was normalized to the respective geometrical electrode area and halved to represent a single lithium-electrolyte interface in the symmetric cell. The impedance data was fitted to an equivalent circuit comprising a high-frequency real resistance R_{hf} in series with a parallel circuit of a constant phase element $CPE_{Li|SE}$ and a resistance $R_{Li|SE}$, accounting for the solid electrolyte in contact with the lithium metal.[38] A python package for electrochemical impedance analysis[90] was utilized for fitting. Due to artifacts prevailing at high and low frequencies regions, the range of data points utilized for fitting was individually adjusted for each impedance spectrum. For the LLZO-based ASSBs, the twelve data points around the maximum absolute impedance value of each spectrum were considered to account for differing time constants of the interface impedance. The fitting frequency range for ASSBs with LPSCl-based solid electrolyte separators was set to 316.2–31.6 kHz.

The liquid electrolyte cells underwent symmetric electrochemical cycling for 25 cycles, with each cycle involving 1 h of dissolution (stripping) and 1 h of deposition (plating) at constant areal currents of 100 µA cm^{-2}. A pause time of 10 min was introduced between the dissolution and deposition steps. Electrochemical impedance spectra were recorded through galvanostatic EIS before each cycle. Again, the measurement points spanned a frequency spectrum of 1 MHz to 100 mHz at an amplitude of 10 mV and were averaged over three measurements.
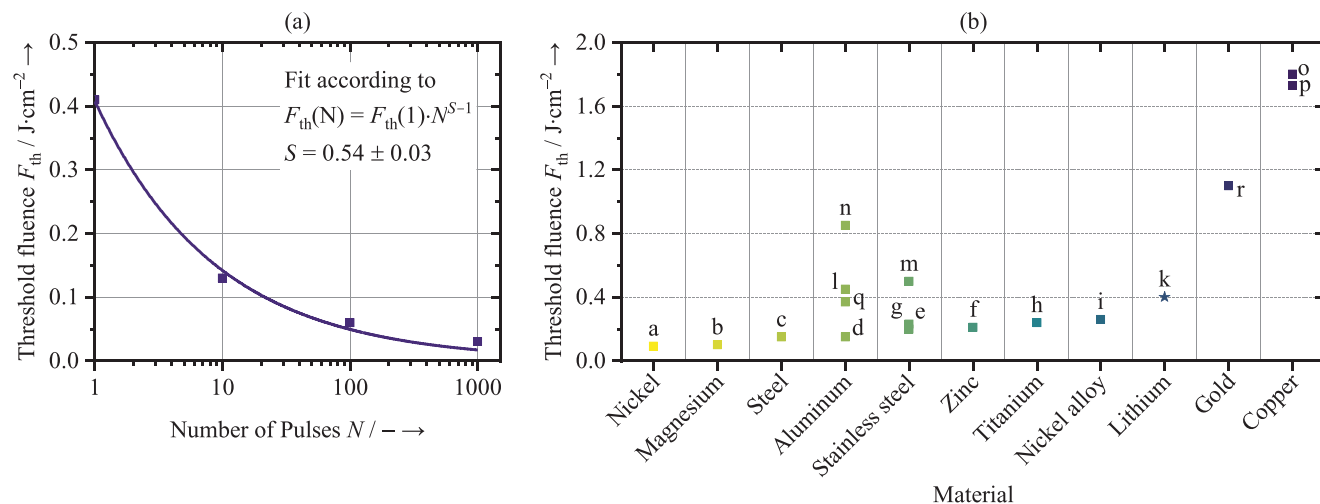
Figure 3. a) The threshold fluences F_{th} of lithium metal for different numbers of applied pulses are depicted. b) Single-pulse ablation thresholds F_{th} of various metals are compiled. Only values obtained at similar boundary conditions (pulse duration τ: 2 – 10 ps, wavelength λ: 1030 – 1070 nm) are included to allow comparability. The single-pulse threshold fluence for lithium metal is marked with a star symbol and the letter k. The literature values are extracted from the following references indicated as letters in plot (b): a:[96]; b:[97]; c, d:[93]; e, l, p:[98]; f:[99]; g:[100]; h, q, r:[101]; i:[102]; m, n, o:[103].

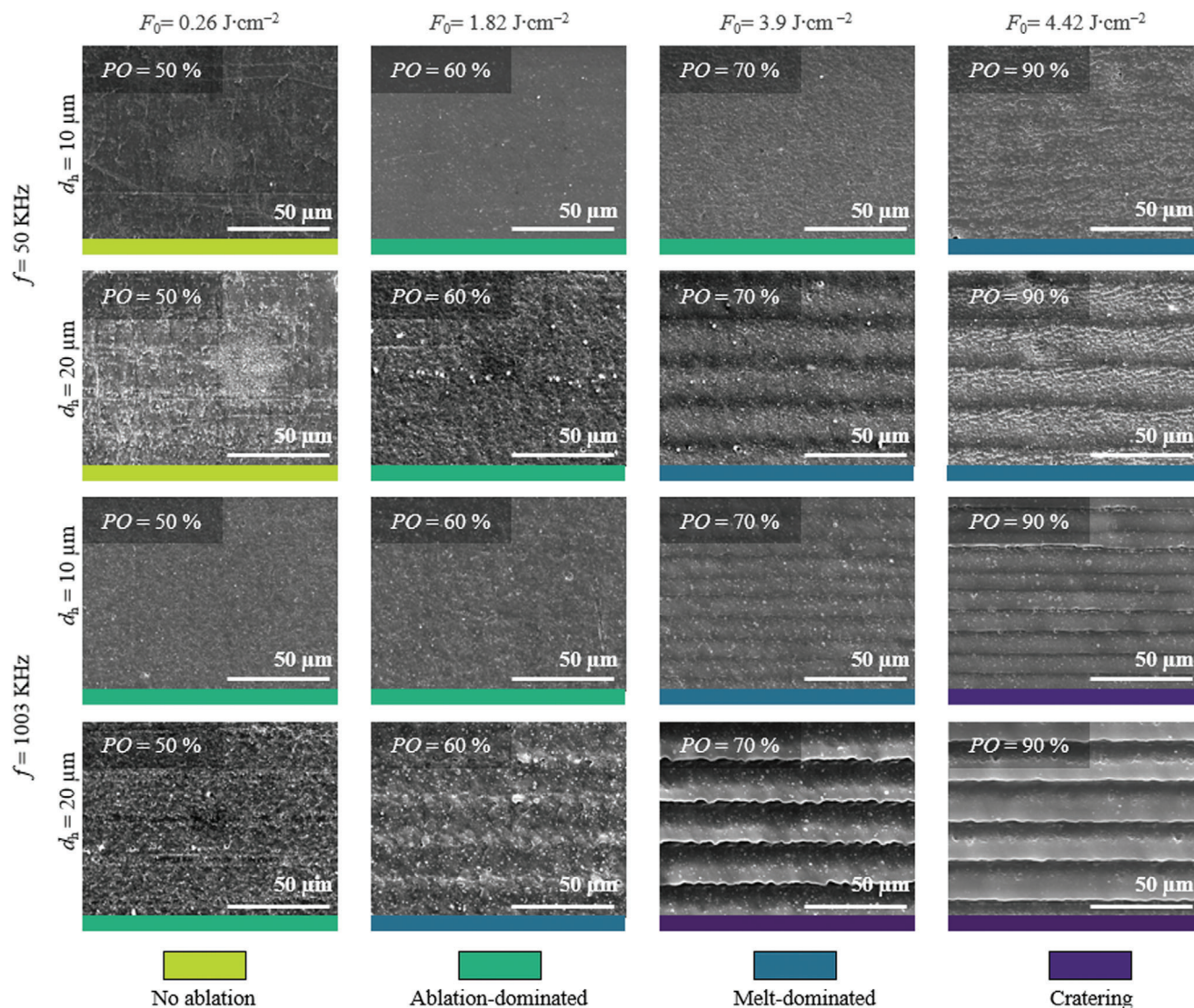## 3. Results and Discussion

3.1. Laser-Based Surface Modification

The performed experiments intended to homogenously ablate a small material fraction from the lithium metal substrate surface. In the first step, single- and multi-pulse threshold fluences for lithium metal had to be experimentally determined since no literature values for picosecond pulse durations were available (see Section S1, Supporting Information). The threshold fluence is a basic laser metric, referring to the minimum peak pulse fluence required for material removal. A single-pulse threshold fluence of 0.41 J cm^{-2} was obtained (**Figure 3a**), which is relatively high compared to literature values for other metals at comparable pulse durations and wavelengths (Figure 3b). Additionally, multi-pulse threshold fluences were investigated since several pulses successively hit the workpiece surface at the same spatial position during areal laser processing, depending on the chosen pulse overlap. It is known that the threshold fluence drops for higher pulse numbers following an incubation power law.[91] This power law is depicted in Figure 3a with threshold fluences of 0.13, 0.06, and 0.03 J cm^{-2} for 10, 100, and 1000 pulses, respectively. These values are significantly below multi-pulse threshold fluences (0.6 – 35.5 J cm^{-2}) previously obtained for lithium metal using nanosecond pulse durations applying 500 pulses.[92] Lithium metal's incubation factor S of 0.54 undershoots those of other metals, such as copper, gold, nickel, and aluminum, which are ≈0.8,[93] suggesting the necessity of a careful process design at high pulse overlaps. A full factorial experimental plan for planar material processing was established based on the ablation threshold to control the surface morphology. In theory, ultrashort-pulsed laser radiation with pico- or femtosecond pulse durations suppresses heat transfer and promotes evaporation-based material removal due to the ultrashort laser-matter interaction time.[94,95] However, as heat accumulation triggered melt for-

mation for some parameter sets, the generated surfaces were assigned to four distinct process regimes, exemplified in **Figure 4**.

If laser radiation failed to modify the surface, the parameter set was categorized into the "no ablation" regime. Material removal failed when peak pulse fluences were below the ablation threshold, and pulse overlaps were insufficient to accumulate heat effectively, as illustrated in the feasibility maps in **Figure 5**.

When surface modification was observed, the samples were classified as "ablation-dominated" or "melt-dominated", depending on the extent of visible melt traces. Typically, higher peak pulse fluences, pulse overlaps, and pulse repetition rates tended to induce melt-dominated behavior, which can be reasoned by promoted heat accumulation at shorter temporal and spatial pulse intervals.[62] Restricting these parameters to lower values led to evaporation-governed material removal, avoiding extensive melt formation. It is important to note that even within the ablation-dominated regime, melting could not be obviated entirely. This might be due to lithium's low melting point of 180.5 °C[24] compared to its evaporation point of 1347 °C,[24] entailing a seamless transition between both regimes. The morphological surface changes induced by laser treatment in the ablation-dominated regime indicate its suitability for laser cleaning. In contrast, heat accumulation during ultrashort-pulsed laser polishing at high pulse repetition rates can be exploited for surface smoothing.[62] Thus, the improved layer-to-layer contact by eliminating surface defects and lowering surface roughness is particularly interesting for ASSBs, reducing the need for annealing steps by pressurization or melting.

Finally, the fourth process regime was designated as the "cratering regime" as melt was dislocated sideways by melt dynamics and vapor recoil pressure, leaving behind surfaces with macroscopic kerf structures. The tendency for groove formation increased with rising temporal, spatial, and pulse-specific energy input in combination with the larger hatch distance of 20 µm. The cratering process regime can be leveraged to create stochastic

**ADVANCED
SCIENCE NEWS**
www.advancedsciencenews.com

**ADVANCED
FUNCTIONAL
MATERIALS**
www.afm-journal.de

Figure 4. Scanning electron microscopy images showing the identified laser process regimes in dependence of the pulse repetition rate f, the pulse fluence F_0, the pulse overlap PO, and the hatch distance d_h are depicted. The laser scan direction was from left to right. A reference parameter set ($F_0 = 1.82$ J cm^{-2}, $f = 50$ kHz, $PO = 60\%$, $d_h = 10$ μm) from the ablation-dominated process regime was selected for the experiments presented in the subsequent sections.
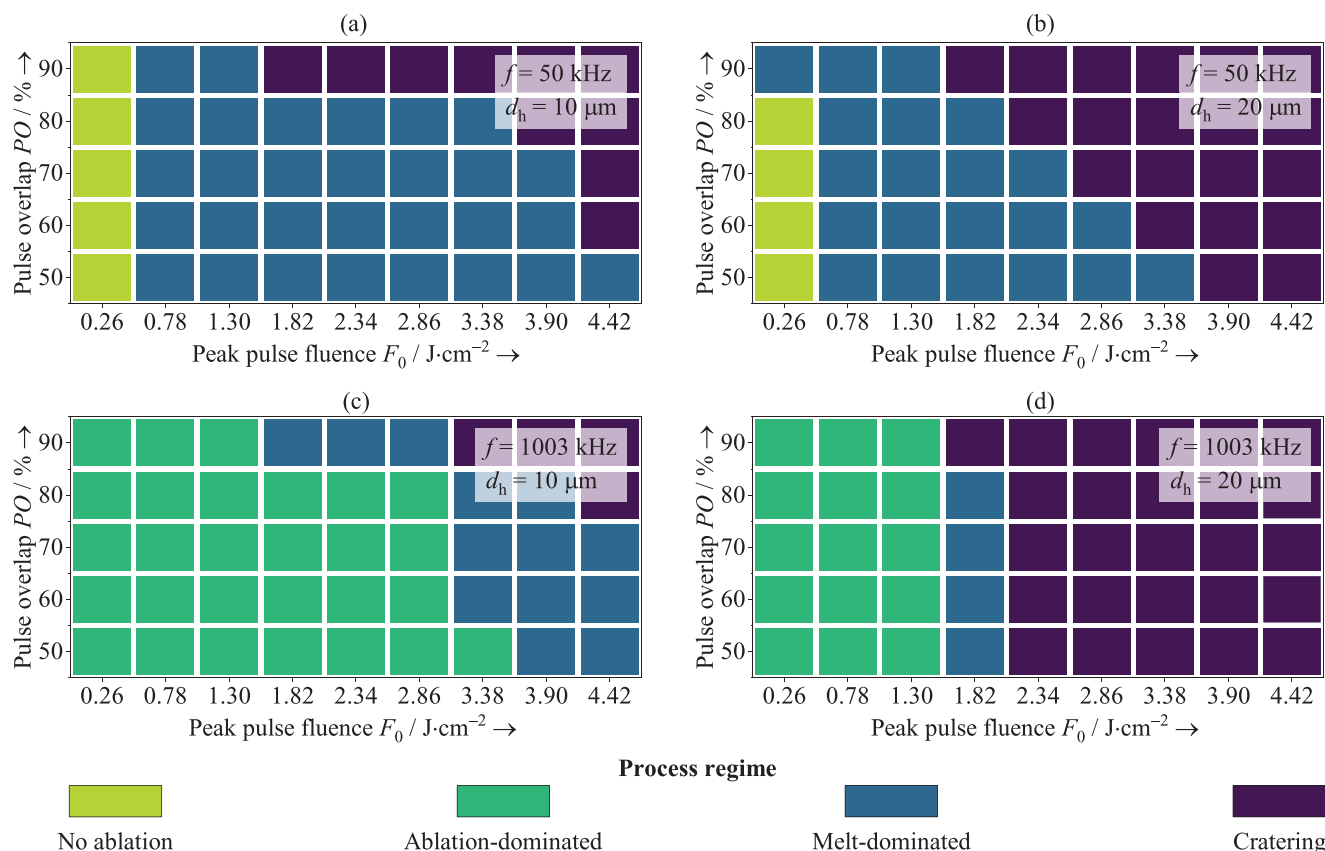
patterns through melt displacement, expanding the surface area (see Section S2, Supporting Information).

The surface roughness Sa of the lithium metal foil following laser treatment varied between 0.15 and 2.30 μm, depending on the applied process parameter set (see Section S3, Supporting Information). Consequently, the surface roughness exhibited the potential for both reduction and elevation compared to the pristine lithium metal foil, which initially had a surface roughness of $Sa = 0.24$ μm. The deliberate laser-induced formation of mazes, bumps, nano-forests, trenches, and chaotic microstructures has already been demonstrated for various metals, such as aluminum, copper, stainless steel, and titanium.[104] Increasing the active surface area analogously to alternative techniques for creating organized[46–48] or chaotic[42] surface structures may prove particularly valuable for liquid-electrolyte bat-

teries, reducing the effective current density at the lithium–electrolyte interface.[42,46,49] It shall be noted that longer pulse durations in the nanosecond range may also be a suitable choice to effect melting and cratering[65] since lithium metal primarily undergoes melting rather than evaporation on that timescale.[105,92]

The remainder of this work concentrates on removing lithium metal surface contaminations by laser cleaning in the ablation-dominated process regime. Therefore, a particular reference parameter set was selected featuring a peak pulse fluence of $F_0 = 1.82$ J cm^{-2}, a pulse repetition rate of $f = 50$ kHz, a pulse overlap of $PO = 60\%$, and a hatch distance of $d_h = 10$ μm. This parameter set unambiguously changed the surface morphology compared to pristine samples, indicating material removal while limiting melt formation.

ADVANCED
SCIENCE NEWS

www.advancedsciencenews.com

ADVANCED
FUNCTIONAL
**MATERIALS**

www.afm-journal.de

Figure 5. The process feasibility maps illustrate the dependence of the occurring process regimes from the pulse overlap PO and the peak pulse fluence F_0 for pulse repetition rates of a,b) $f = 50$ kHz and c,d) $f = 1003$ kHz in combination with (a,c) hatch distances of (a,c) $d_h = 10$ µm and (b,d) $d_h = 20$ µm.

3.2. Removal of Surface Contaminants

Next, the feasibility of laser cleaning for removing contaminants from the lithium metal surface was investigated. For this purpose, the reference parameter set was applied with up to four consecutive passes, adjusting the scan direction by 90° after every laser cleaning cycle, as exemplified in the protocol of Figure 2. While multi-step laser micro-polishing usually targets a step-wise

reduction of the surface roughness,[106] the primary objective in these experiments was to gradually reduce oxygen and carbon residues on the substrate surface. However, microstructural surface imperfections like scratches were progressively eliminated with each pass, and the directionality of the surface features diminished as continuous rescanning merged neighboring microbumps (**Figure 6**, top row).[104,106] Additionally, lithium metal substrates were exposed to ambient conditions (dew point ≈5 °C)
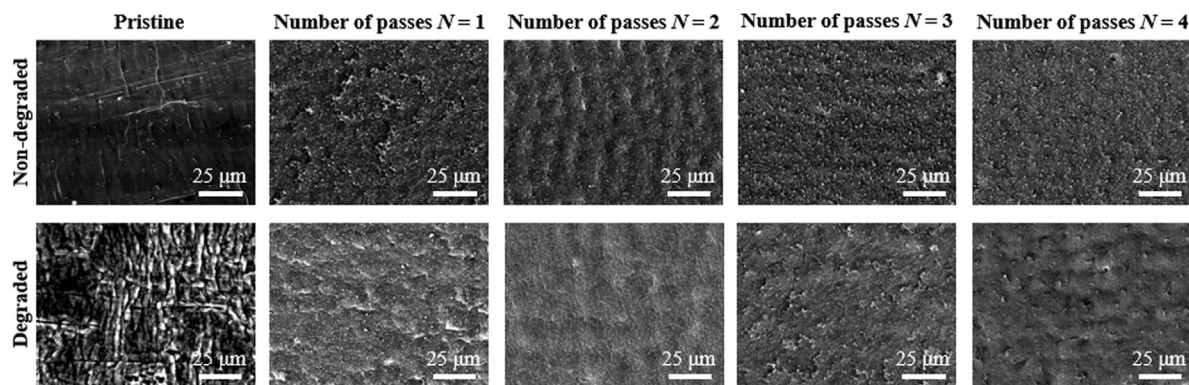
Figure 6. Scanning electron microscopy images of (top row) pristine and (bottom row) degraded lithium metal surfaces with 0 – 4 laser passes are displayed. The laser scan direction was from left to right for one pass and adjusted by 90° after every laser cleaning cycle for the multi-pass strategies to reduce the directionality of the resulting surface patterns.

**ADVANCED
SCIENCE NEWS**

www.advancedsciencenews.com

**ADVANCED
FUNCTIONAL
MATERIALS**

www.afm-journal.de
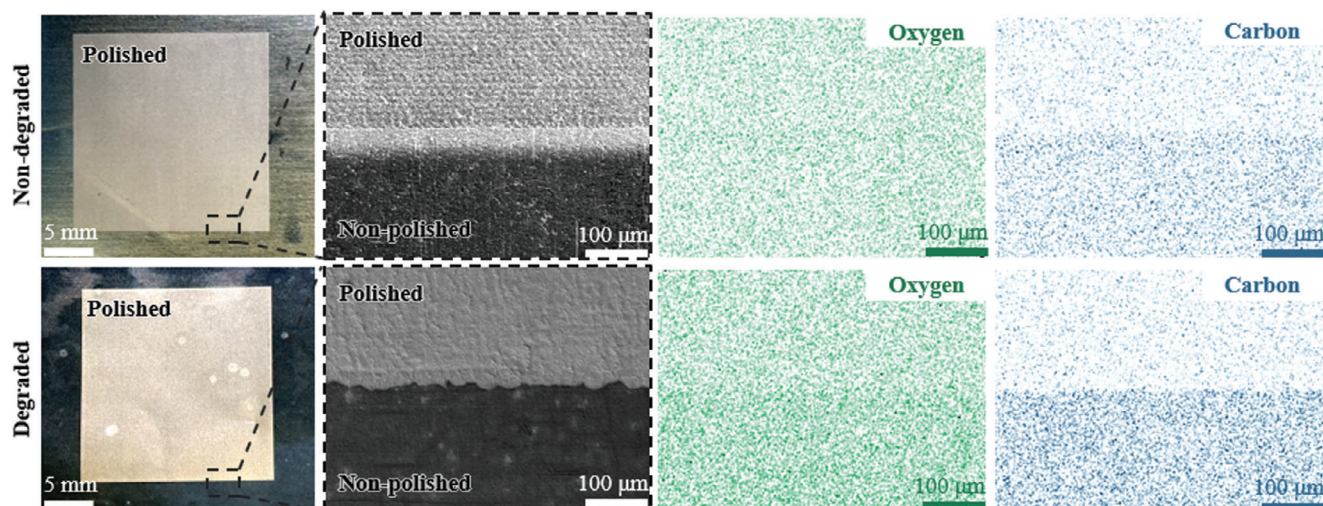
Figure 7. Light images, scanning electron microscopy (SEM) images, and energy-dispersive X-ray spectroscopy (EDX) mappings of oxygen and carbon at the transition between a laser-treated (top part) and an untreated (bottom part) surface area for a non-degraded and a degraded lithium substrate are shown. The EDX acceleration voltage was 1 kV.

for ten minutes to intentionally trigger the formation of a distinct passivation layer (see Section S4, Supporting Information). Seo et al. (2022) determined a contamination layer growth rate of 24 nm•min^{-1} on fresh lithium metal using optical spectroscopic ellipsometry, which suggests that the formed contamination layer in this experiment surpasses 100 nm.[107] Strong degradation traces in the form of lamellar surface structures were observed on the degraded samples. However, laser treatment successfully removed these structures, reestablishing a planar surface (Figure 6, bottom row).

Areal EDX maps were recorded to visualize the levels of oxygen and carbon present on the surface (**Figure 7**). Lithium is not represented in these maps due to the limitations of standard EDX in detecting elements with low atomic numbers. Despite this, one can consider EDX mapping for carbon and oxygen as indicators for surface contaminations. The carbon content was evidently reduced in the laser-treated regions of both the degraded and non-degraded samples. Moreover, laser cleaning decreased oxygen fractions, particularly on the degraded samples, underlining the success of the presented method. These findings align well with results from Wolf et al. (2021), who reported a preferential reduction of carbonate species by sandblasting.[42]

A possible rationale is that carbon compounds are primarily located in the outermost surface layer, which is mainly measured at an acceleration voltage of 1 kV. Additionally, lithium carbonate forms relatively slowly compared to oxygen compounds, which makes it reasonable to expect a reduced amount of carbon on freshly exposed lithium surfaces and accords with observations in Refs. [108,27]. In contrast, the freshly excavated lithium metal may be susceptible to rapid oxygen passivation due to atmospheric contaminations in the glovebox and transport module as well as during insertion in the SEM, where it was briefly exposed to dry air, even if only for a maximum of five minutes.[109]

In the following steps, count maps were generated at various acceleration voltages up to 5 kV for quantitative analysis to investigate the material composition in deeper regions by successively increasing the measurement depth (**Figure 8**). According to Otto
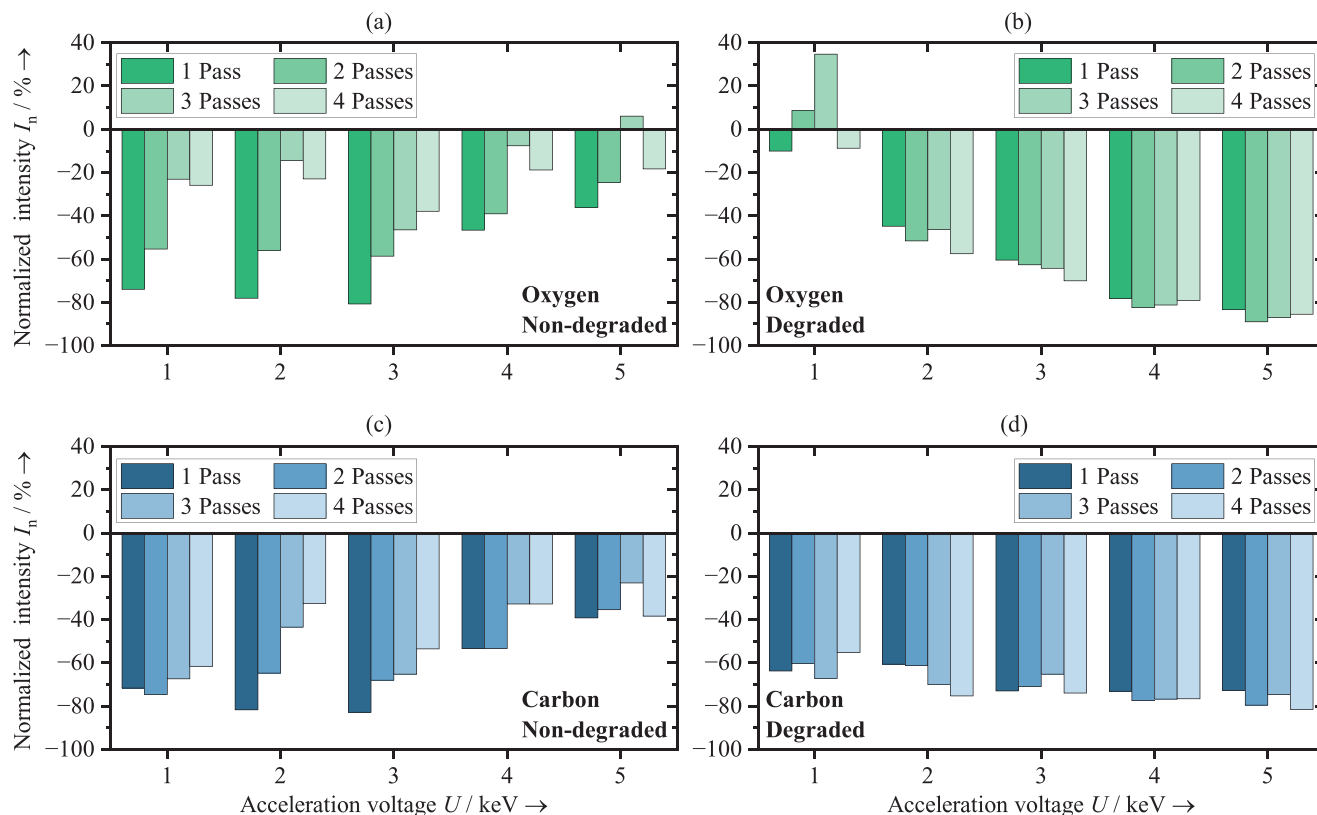
et al., an acceleration voltage of 5 kV corresponds to an average penetration depth of ≈800 nm.[28] The absolute counts for oxygen were significantly higher for the degraded compared to the non-degraded lithium metal substrates before laser treatment, accounting for a more pronounced surface layer. For instance, the oxygen counts for the non-degraded and degraded samples at an acceleration voltage of 5 kV were 2940 and 20 000, respectively (Section S5, Supporting Information). The oxygen and carbon counts on the laser-treated samples were referenced to the values of the untreated samples at the respective acceleration voltages to assess relative changes in the surface composition (Figure 8).

Except for oxygen at the lowest acceleration voltage of 1 kV on the degraded sample, surface contaminants were significantly reduced in all configurations. When testing the non-degraded substrates, a significant drop in oxygen and carbon was noticeable at lower acceleration voltages (1 – 3 keV). Specifically, oxygen decreased by up to 81% and carbon by up to 83%, both at an acceleration voltage of 3 keV and one laser pass (Figure 8a,c).

Intense signals at higher acceleration voltages for the degraded samples confirm the presence of thicker passivation films. Consistent carbon diminutions ≈60 – 80% were detected across all acceleration voltages on the degraded samples (Figure 8d). In contrast, a more prominent lowering of oxygen traces occurred at higher acceleration voltages, indicating the reformation of a thin layer of oxidic compounds after laser treatment. Applying multiple passes did not yield a detectable oxygen or carbon reduction within the conducted experiments. The measurement routine in the EDX might be the reason for this, as the one-pass samples were initially analyzed, and sample degradation cannot be excluded even in high vacuum and with short measuring times.

3.3. Electrochemical Analysis

Laser-treated lithium metal electrodes were integrated into symmetrical ASSBs to assess their chemical stability under electrochemical testing conditions. In this context, LLZO and LPSCl

ADVANCED
SCIENCE NEWS

www.advancedsciencenews.com

ADVANCED
FUNCTIONAL
MATERIALS

www.afm-journal.de

Figure 8. Normalized count intensities I_n of a,b) oxygen and c,d) carbon as a function of the electron acceleration voltage are shown for (a,c) a non-degraded and (b,d) a degraded sample. The counts measured for the laser-treated samples I_{po} are normalization to the counts measured for a non-modified sample at the same acceleration voltage I_{pr} according to $I_n = 1 - \frac{I_{po}}{I_{pr}}$. Thus, a negative value for I_n signifies a reduction of the respective element by laser treatment.

were chosen as showcase solid electrolyte separator materials. In contact with lithium metal, LLZO generally exhibits a high chemical stability,[110,111] whereas LPSCl forms compounds such as Li_2S.[112,9] EIS was applied to measure the effect of the laser treatment of lithium metal electrodes on the interfacial resistances in contact with solid electrolytes. This experiment primarily focused on demonstrating the impact of reduced carbonaceous and oxidic species, as confirmed by EDX in the preceding section, on the interfacial resistances rather than optimizing the electrochemical battery performance.
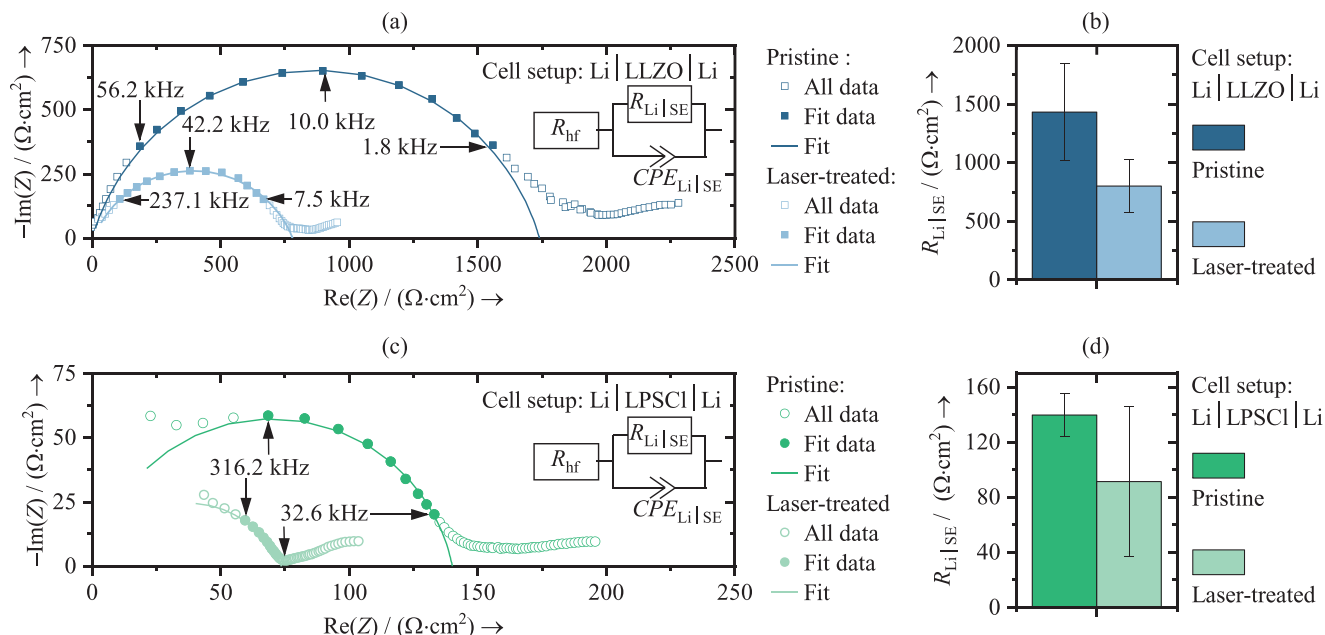
The normalized electrochemical impedance spectra of LLZO-based and LPSCl-based symmetric ASSBs at open circuit voltage (OCV) conditions are exemplified in **Figure 9a,c**, respectively. No distinct electrolyte bulk and grain boundary resistances appeared in the high frequency region ($R_{hf} \approx 0\ \Omega\ cm^2$) due to superposition with the interface resistances. However, by assuming that the electrolyte resistances remain constant and are not affected by laser treatment, changes in $R_{Li|SE}$ can be attributed to altered interface resistances.

Values for $R_{Li|SE}$ were obtained by fitting an equivalent circuit model to the measurement data of several symmetric ASSBs. Average $R_{Li|SE}$ values for ASSBs with LLZO and LPSCl solid electrolyte separators, including error intervals, are comprised in Figure 9b,c, respectively. Laser treatment notably reduced $R_{Li|SE}$ from 1433 ± 411 to $801 \pm 223\ \Omega\ cm^2$ ($\approx44\%$) for the LLZO-

based and 139 ± 15 to $91 \pm 54\ \Omega\ cm^2$ ($\approx35\%$) for the LPSCl-based ASSBs compared to similar cell architectures with pristine lithium metal electrodes. The rather high interfacial resistances for LLZO can be traced back to the omission of dedicated annealing measures aimed at avoiding any impact on the electrode–electrolyte interface. Typically such steps are applied to reduce the interfacial resistances and, amongst others, involve isostatic pressing at high external pressures of several hundred megapascals,[113,114,32] heating,[111,115] or melting.[116] For comparative impedance data, the reader is referred to prior literature on ASSBs with LLZO[117–120,32] and LPSCL[112,121,82] separators.

It is concluded that the substantially reduced interfacial resistances can be traced back to the passivation layer removal through the laser treatment approach introduced in this paper, exposing pristine lithium metal toward a solid electrolyte selected to either be a lithium garnet oxide, such as LLZO, or a lithium argyrodite sulfide, such as LPSCl, compound.

To mitigate the influence of the electrode–electrolyte interfacial contact inherent to cells with solid electrolytes, the electrochemical results obtained in ASSBs were complemented with those from lithium metal batteries using a liquid electrolyte. **Figure 10a** depicts the overvoltages observed during the symmetrical cycling of a cell with pristine lithium metal anodes and a cell with laser-treated electrodes. The overvoltages, representing the cell voltage accounting for both electrodes, align well with

ADVANCED
SCIENCE NEWS
www.advancedsciencenews.com

ADVANCED
FUNCTIONAL
MATERIALS
www.afm-journal.de

Figure 9. Exemplary Nyquist plots of symmetric all-solid-state batteries (ASSBs) with laser-treated and pristine lithium metal anodes combined with a) an LLZO and c) an LPSCl solid electrolyte separator are displayed. The relevant frequencies for the fitting procedure are labeled. The data is normalized to the surface area of one interface in the symmetric cell. A high-frequency resistance (R_{hf}) in series with a parallel circuit of another resistance ($R_{Li|SE}$) and a constant phase element ($CPE_{Li|SE}$) were used as equivalent circuits for the fitting procedure. The average resistances $R_{Li|SE}$ of symmetric ASSBs incorporating laser-treated or pristine lithium metal anodes with b) LLZO and d) LPSCl separators are depicted. The error bars account for the standard deviation of three cells in each case. No degradation procedure was applied to the lithium metal anodes tested in these experiments.

the voltage range reported in the literature for similar experimental setups.[41,42] Notably, the laser-treated cell exhibits lower and more consistent overvoltages compared to its pristine counterpart. This behavior aligns closely with findings reported by Becking et al. (2017),[41] who utilized a calendaring step to thin the native surface film, and Wolf et al. (2021),[42] who employed abrasive blasting for surface film removal.

In Figure 10b, Nyquist plots for both cells recorded under OCV conditions in the initial state, after the 1st cycle, and after the 25th

cycle are presented. The impedance of the laser-treated cell remains relatively constant throughout the cycles, contrasting with the significant decrease in impedance observed for the pristine cell after the first cycle. In the initial cycle, the native surface film predominantly influences the impedance, but as cycling progresses, changes in the surface morphology and chemistry of the lithium electrodes occur due to continuous lithium dissolution and deposition.[41] The creation of fresh lithium surfaces during cycling diminishes the impact of the native film. The lower initial
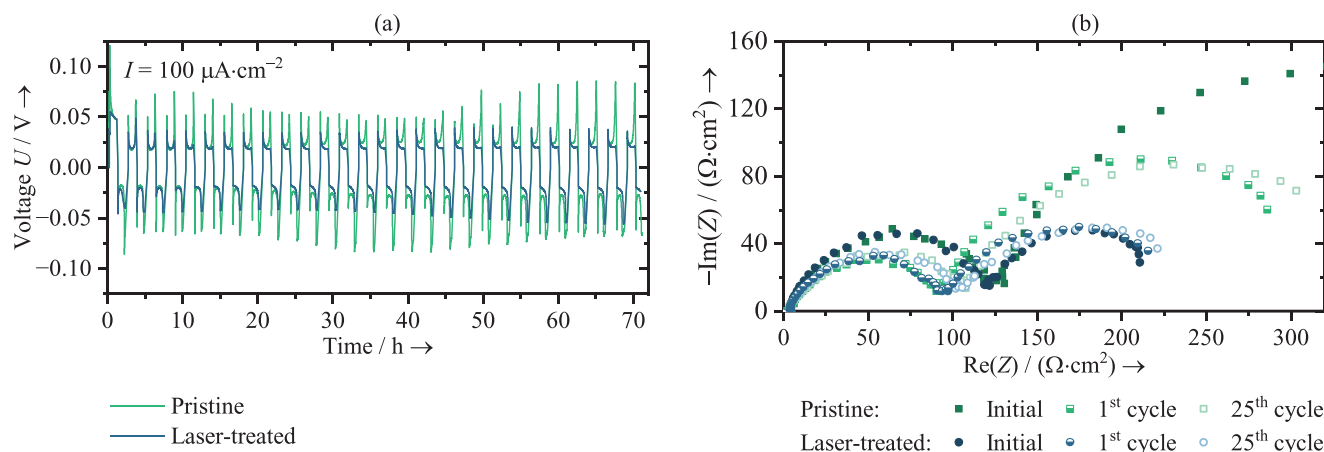
Figure 10. The electrochemical testing results for symmetric lithium metal batteries with a liquid electrolyte are presented. a) The voltage profiles of a cell containing pristine electrodes and a cell containing laser-treated electrodes during symmetrical cycling at constant areal currents of $I = \pm 100 \, \mu A \, cm^{-2}$ over 25 dissolution–deposition cycles. b) Nyquist plot showing the impedance data for the initial state, the 1st cycle, and the 25th cycle of the pristine and the laser-treated cell.

RIGHTSLINK()

ADVANCED
SCIENCE NEWS

www.advancedsciencenews.com

ADVANCED
FUNCTIONAL
MATERIALS

www.afm-journal.de
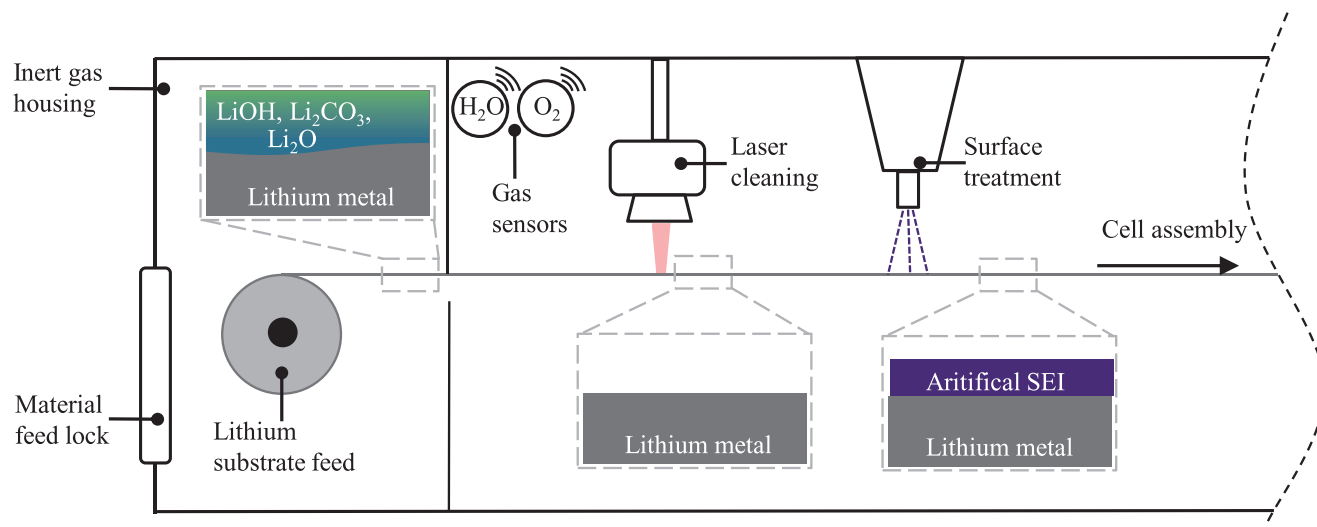
Figure 11. An integration concept for laser cleaning of lithium metal substrates in battery production is schematically displayed. The state of the lithium metal surface is indicated in the insets. Applying an artificial solid electrolyte interphase (SEI) after laser treatment can involve various electrochemical, chemical, or physical methods.[44]

impedance of the laser-treated cell supports the hypothesis that the native surface film was partially removed or reduced in its thickness. The impedance remained higher for the pristine cell compared to the laser-treated cell also after 25 cycles. With ongoing cell operation, the absolute impedance, accounting for the native surface film and the SEI formed by the contact of fresh lithium metal with liquid electrolyte, is increasingly dominated by the newly deposited lithium.[42] It is postulated that SEI formation is influenced by the composition of the native surface film before cycling, potentially contributing to enhanced electrochemical performance for the laser-treated cell, manifested in lower overvoltages and a reduced cell impedance.

Becking et al. (2017) substantiated their findings through post-mortem X-ray photoelectron spectroscopy(XPS) and SEM analyses, demonstrating that the thinning of the native surface film leads to alterations in electrode morphology and SEI chemistry.[41] These surface changes are considered advantageous factors contributing to the extension of cell lifetime, providing insight into a similar behavior for the cells presented in this study.

3.4. Industrial Practicability Study

Industrially producing lithium metal batteries requires slitting and contour cutting by laser radiation to generate anodes from the roll goods delivered from foil suppliers.[122,123] Employing laser-based surface modification prior to anode singulation, cell stacking, and packaging limits the time for the ongoing passivation layer reformation.[28] At this juncture, cell manufacturers may also superimpose their proprietary artificial surface layers for passivation or tailoring the lithium metal substrate surface to align with their specific cell chemistry, especially with respect to the employed solid or liquid electrolyte.

Moreover, laser treatment reduces the necessity of a high-purity atmosphere to the process steps from surface modification

to cell assembly. As surface contaminants can be removed, processing and handling steps preceding laser treatment may be performed at less demanding environmental conditions, such as dry air, reducing expenses. A conceptual depiction of the implementation of laser-based surface modification within the manufacturing chain for lithium metal batteries is illustrated in **Figure 11**.

Embedding the laser parameters identified in the preceding sections of this publication in a production scenario with a lithium foil substrate width of 70 mm and a roll-to-roll feed rate of 6 m min^{-1}, i.e., a material throughput of 0.42 m min^{-1}, allows to calculate a necessary scanning speed to confirm to the targeted hatch distance (**Table 2**).

The requested scanning speed of 700 m·s^{-1} perpendicular to the substrate feed direction can be served by highly dynamic

Table 2. A scenario for the industrial implementation of laser surface treatment of lithium metal substrates in a roll-to-roll process is modeled. The scenario parameters are based on reasonable assumptions in the context of industrial battery production. The assumed laser parameters are adopted from the experimental results presented in the preceding sections of this work. The required laser system parameters are calculated. For reasons of simplification, a scanner utilization efficiency of 100% is assumed, disregarding laser-off-times when switching between polygon facets.

Scenario parameters	Substrate feed rate s/(m min^{-1})	6
	Foil width b/mm	70
	Material throughput TP/(m^2 min^{-1})	0.42
Assumed laser parameters	Pulse peak fluence F_0/(J cm^{-2})	1.82
	Pulse energy E_p/μJ	8.75
	Pulse overlap PO/%	60
	Focal radius w_0/μm	17.5
	Hatch distance h_d/μm	10
Required laser system parameters	Scanning speed v/(m s^{-1})	700
	Pulse repetition rate f/MHz	50
	Average laser power P/W	437.5

ADVANCED
SCIENCE NEWS

www.advancedsciencenews.com

**ADVANCED
FUNCTIONAL
MATERIALS**

www.afm-journal.de

polygon scanning units, incorporating a constantly moving polygon wheel for a one-directional beam deflection.[124,125] Such polygon scanning units were already implemented for laser micro-processing, achieving material throughputs up to 0.77 m^2 min^{-1}.[125] Moreover, multibeam processing might be a feasible alternative to reach high material throughputs.[126]

The necessary pulse repetition rate can be calculated using the desired pulse overlap (see Equation 4). Within the modeled scenario results, the required pulse repetition rate is 50 MHz, resulting in an average laser power of 437.5 W to deliver pulse energies of 8.75 µJ (Equation 3). Picosecond laser beam sources meeting these requirements are scientifically established and commercially available,[127] confirming the industrial practicability of the demonstrated laser process. As a consequence, the high scalability of the laser-based surface modification allows its integration into roll-to-roll industrial battery production chains. The estimated process costs for lithium metal laser cleaning, based on the calculated material throughput of 0.42 m^2 min^{-1}, are 0.93 US\$ m^{-2} according to production cost modeling for a facility situated in Germany (Section S6, Supporting Information). In consideration of a lithium foil price of 1000 US\$ kg^{-1} for foil thicknesses below 100 µm,[35] these costs constitute less than 9% and 4% of the total price of 10.64 US\$ m^{-2} for 20 and 50 µm foils, respectively. It is anticipated that the expenses associated with laser cleaning could be even lower in production sites with reduced labor and energy costs. Additionally, improving the process design to increase the material throughput and an expected reduction of the investment costs for laser system components further alleviates the overall cost burden of laser cleaning.

4. Conclusion

A low interfacial resistance enabled by precisely controlling the passivation levels at the interface between lithium metal electrodes and solid electrolytes is a key performance metric to unlock ASSBs with increased energy densities compared to conventional lithium-ion batteries. To date, research has predominantly considered treating lithium metal substrates with non-scalable and rather manual methods, hampering the transfer to scale on industrial production lines. In contrast, a unique laser setup in a controlled environment was constructed in this study to investigate the capability of pulsed laser treatment for removing superficial contaminants on delicate lithium metal substrates, ultimately improving the interface toward solid electrolytes. The presented approach represents an extension to lithium metal battery manufacturing by providing finer control and greater efficiency in lithium surface manipulation, aiming at diminished interfacial resistances and elevated fast charging capabilities in ASSBs.

To this end, various laser process regimes were explored using the custom-designed laser module to tailor the surface properties of lithium metal substrates. While the precise adjustability of the laser process facilitates the creation of a multitude of morphological and chemical surface conditions, an ablation-based laser process regime was selected, concentrating on modifying the chemical nature of lithium metal substrates. EDX revealed a decrease of oxygen and carbon on laser-treated lithium metal surfaces by ≈80%. Besides, it was shown that even heavy surface contaminations on lithium metal substrates stemming from subjection to ambient air can be significantly reduced, predicting a pathway

for the reconditioning of degraded material. Symmetric ASSBs using separators from two of the most impactful inorganic solid electrolytes were manufactured to validate the efficacy of the laser treatment. It was confirmed that removing the passivation layer reduced initial interface impedances in the symmetric battery cells comprising lithium garnet oxide and argyrodite sulfide solid electrolytes by 44% and 35%, respectively. The promising chemical and electrochemical results point to the effectiveness of the laser treatment.

Collectively, the low laser pulse energies required for the surface treatment ≈1.8 J cm^{-2}, together with high pulse repetition rates in the MHz range offered by modern laser sources, hold potential for implementing the proposed method into industrial roll-to-roll production lines. Compared to alternative methods, the laser-based approach offers the advantage of being free of mechanical impact, allowing for the processing of thin and delicate substrates required for reaching high-energy lithium metal batteries.

Future work requires the exploitation of complementary characterization techniques such as XPS and time-of-flight secondary ion mass spectrometry (see Section S7, Supporting Information). Furthermore, to deepen insights into the evolution of interface layers, it is recommended to conduct additional electrochemical testing of laser-cleaned lithium metal anodes. These experiments should encompass both symmetric and full cells, incorporating liquid and solid electrolytes to unravel the dynamic processes at the electrode-electrolyte interface. Thereby, tailoring the surface chemistry of lithium metal substrates to the aspired cell design by superimposing proprietary artificial protective layers directly after laser cleaning offers a promising pathway for manufacturing improved lithium metal batteries.

Supporting Information

Supporting Information is available from the Wiley Online Library or from the author.

Conflict of Interest

Two of the authors, H.B. and J.K., recently filed an up-to-now non-disclosed patent on the method that is scientifically described in the publication. However, the patent does not contain any of the data shown in the research paper but only a general description of the method. Thus, the research paper can be seen as scientific extension to the patent.

Author Contributions

J.K. performed conceptualization, methodology, investigation, visualization, formal analysis, data curation, validation, wrote the original draft, wrote, review, and edited the draft. H.B. performed conceptualization, investigation, wrote, review, and edited the draft. S.D. performed investigation, data curation. A.G.D. performed conceptualization, wrote, review,

**ADVANCED
SCIENCE NEWS**

www.advancedsciencenews.com

**ADVANCED
FUNCTIONAL
MATERIALS**

www.afm-journal.de

and edited the draft. L.H. performed wrote, review, and edited the draft. Y.L. performed investigation. L.W. S.W., and K.J.K. provided resources and performed wrote, review, and edited the draft. J.K. performed data curation, software. J.L.M.R. performed conceptualization, wrote, review and edited the draft, and provided resources. M.F.Z. performed supervision, project administration, funding acquisition, wrote, review, and edited the draft.

Data Availability Statement

The data that support the findings of this study are available from the corresponding author upon reasonable request.

Keywords

[1] G. Zubi, R. Dufo-López, M. Carvalho, G. Pasaoglu, *Renewable Sustainable Energy Rev.* **2018**, *89*, 292.

[2] T. Placke, R. Kloepsch, S. Duehnen, M. Winter, *J. Solid State Electrochem.* **2017**, *21*, 1939.

[3] J. Janek, W. G. Zeier, *Nat. Energy* **2016**, *1*, 16141.

[4] C. Bauer, S. Burkhardt, N. P. Dasgupta, L. A.-W. Ellingsen, L. L. Gaines, H. Hao, R. Hischier, L. Hu, Y. Huang, J. Janek, C. Liang, H. Li, J. Li, Y. Li, Y.-C. Lu, W. Luo, L. F. Nazar, E. A. Olivetti, J. F. Peters, J. L. M. Rupp, M. Weil, J. F. Whitacre, S. Xu, *Nat. Sustain.* **2022**, *5*, 176.

[5] D. Lin, Y. Liu, Y. Cui, *Nat. Nanotechnol.* **2017**, *12*, 194.

[6] P. G. Bruce, S. A. Freunberger, L. J. Hardwick, J.-M. Tarascon, *Nat. Mater.* **2011**, *11*, 19.

[7] A. Varzi, K. Thanner, R. Scipioni, D. Di Lecce, J. Hassoun, S. Dörfler, H. Altheus, S. Kaskel, C. Prehal, S. A. Freunberger, *J. Power Sources* **2020**, *480*, 228803.

[8] M. Balaish, J. C. Gonzalez-Rosillo, K. J. Kim, Y. Zhu, Z. D. Hood, J. L. M. Rupp, *Nat. Energy* **2021**, *6*, 227.

[9] K. J. Kim, M. Balaish, M. Wadaguchi, L. Kong, J. L. M. Rupp, *Adv. Energy Mater.* **2021**, *11*, 2002689.

[10] S. Dörfler, H. Althues, P. Härtel, T. Abendroth, B. Schumm, S. Kaskel, *Joule* **2020**, *4*, 539.

[11] L. Grande, E. Paillard, J. Hassoun, J.-B. Park, Y.-J. Lee, Y.-K. Sun, S. Passerini, B. Scrosati, *Adv. Mater.* **2015**, *27*, 784.

[12] D. Andre, H. Hain, P. Lamp, F. Maglia, B. Stiaszny, *J. Mater. Chem. A* **2017**, *5*, 17174.

[13] A. Shellikeri, V. Watson, D. Adams, E. E. Kalu, J. A. Read, T. R. Jow, J. S. Zheng, J. P. Zheng, *J. Electrochem. Soc.* **2017**, *164*, A3914.

[14] J. H. Cho, K. Kim, S. Chakravarthy, X. Xiao, J. L. M. Rupp, B. W. Sheldon, *Adv. Energy Mater.* **2022**, *12*, 2200369.

[15] J. Liu, Z. Bao, Y. Cui, E. J. Dufek, J. B. Goodenough, P. Khalifah, Q. Li, B. Y. Liaw, P. Liu, A. Manthiram, Y. S. Meng, V. R. Subramanian, M. F. Toney, V. V. Viswanathan, M. S. Whittingham, J. Xiao, W. Xu, J. Yang, X.-Q. Yang, J.-G. Zhang, *Nat. Energy* **2019**, *4*, 180.

[16] M. Genovese, A. J. Louli, R. Weber, S. Hames, J. R. Dahn, *J. Electrochem. Soc.* **2018**, *165*, A3321.

[17] C. Niu, D. Liu, J. A. Lochala, C. S. Anderson, X. Cao, M. E. Gross, W. Xu, J.-G. Zhang, M. S. Whittingham, J. Xiao, J. Liu, *Nat. Energy* **2021**, *6*, 723.

[18] X. Zhang, A. Han, Y. Yang, *J. Mater. Chem. A* **2020**, *8*, 22455.

[19] P. Bouchard, P.-E. Guerin, G. Laroche, G. St-Amant, *European patent (EP0692831B1)*, **1999**.

[20] B. Stumper, J. Dhom, L. Schlosser, D. Schreiner, A. Mayr, R. Daub, *Proc. CIRP* **2022**, *107*, 984.

[21] D. Vanleeuw, D. Sapundjiev, G. Sibbens, S. Oberstedt, P. Salvador Castiñeira, *J. Radioanal. Nucl. Chem.* **2014**, *299*, 1113.

[22] A. S. Ho, A. S. Westover, K. Browning, J. A. Maslyn, D. Y. Parkinson, R. Sahore, N. Dudney, N. P. Balsara, *ACS Energy Lett.* **2022**, *7*, 1120.

[23] K. Schönherr, B. Schumm, F. Hippauf, R. Lissy, H. Althues, C. Leyens, S. Kaskel, *Chem. Eng. J. Adv.* **2022**, *9*, 100218.

[24] D. W. Jeppson, J. L. Ballif, W. W. Yuan, B. E Chou, *Lithium Literature Review: Lithium's Properties and Interactions*, Hanford Engineering Development Lab., Richland, USA, **1978**.

[25] I. Ismail, A. Noda, A. Nishimoto, M. Watanabe, *Electrochim. Acta* **2001**, *46*, 1595.

[26] R. Schmitz, R. Müller, S. Krüger, R. W. Schmitz, S. Nowak, S. Passerini, M. Winter, C. Schreiner, *J. Power Sources* **2012**, *217*, 98.

[27] A. Etxebarria, D.-J. Yun, M. Blum, Y. Ye, M. Sun, K.-J. Lee, H. Su, M. Á. Muñoz-Márquez, P. N. Ross, E. J. Crumlin, *ACS Appl. Mater. Interfaces* **2020**, *12*, 26607.

[28] S.-K. Otto, Y. Moryson, T. Krauskopf, K. Peppler, J. Sann, J. Janek, A. Henss, *Chem. Mater.* **2021**, *33*, 859.

[29] K. Morigaki, A. Ohta, *J. Power Sources* **1998**, *76*, 159.

[30] S. Shiraishi, K. Kanamura, Z.-I. Takehara, *J. Appl. Electrochem.* **1999**, *29*, 867.

[31] C. Naudin, J. L. Bruneel, M. Chami, B. Desbat, J. Grondin, J. C. Lassègues, L. Servant, *J. Power Sources* **2003**, *124*, 518.

[32] S.-K. Otto, T. Fuchs, Y. Moryson, C. Lerch, B. Mogwitz, J. Sann, J. Janek, A. Henss, *ACS Appl. Energy Mater.* **2021**, *4*, 12798.

[33] E. P. Kamphaus, S. Angarita-Gomez, X. Qin, M. Shao, M. Engelhard, K. T. Mueller, V. Murugesan, P. B. Balbuena, *ACS Appl. Mater. Interfaces* **2019**, *11*, 31467.

[34] Y. He, X. Ren, Y. Xu, M. H. Engelhard, X. Li, J. Xiao, J. Liu, J.-G. Zhang, W. Xu, C. Wang, *Nat. Nanotechnol.* **2019**, *14*, 1042.

[35] R. Schmuch, R. Wagner, G. Hoerpel, T. Placke, M. Winter, *Nat. Energy* **2018**, *3*, 267.

[36] B. T. Dover, C. W. Kamienski, R. C. Morrison, T. J. R. Currin, J. A. Schwindeman, *United States Patent (5,776,369)*, **1998**.

[37] U. Wietelmann, C. Hartnig, U. Emmel, S. Schroeter, *European patent (EP 2 802 429 B1)*, **2018**.

[38] P. Bron, B. Roling, S. Dehnen, *J. Power Sources* **2017**, *352*, 127.

[39] L. Gireaud, S. Grugeon, S. Laruelle, B. Yrieix, J.-M. Tarascon, *Electrochem. Commun.* **2006**, *8*, 1639.

[40] J. Liang, X. Li, Y. Zhao, L. V. Goncharova, W. Li, K. R. Adair, M. N. Banis, Y. Hu, T.-K. Sham, H. Huang, L. Zhang, S. Zhao, S. Lu, R. Li, X. Sun, *Adv. Energy Mater.* **2019**, *9*, 1902125.

[41] J. Becking, A. Gröbmeyer, M. Kolek, U. Rodehorst, S. Schulze, M. Winter, P. Bieker, M. C. Stan, *Adv. Mater. Interfaces* **2017**, *4*, 1700166.

[42] A. Wolf, H. Lorrmann, A. Flegler, A. J. Wolf, A. Guerfi, K. Mandel, G. A. Giffin, *Energy Technol.* **2021**, *9*, 2100455.

[43] R. Xu, X.-B. Cheng, C. Yan, X.-Q. Zhang, Y. Xiao, C.-Z. Zhao, J.-Q. Huang, Q. Zhang, *Matter* **2019**, *1*, 317.

[44] N. Delaporte, Y. Wang, K. Zaghib, *Front. Mater.* **2019**, *6*, 267.

[45] K. N. Wood, M. Noked, N. P. Dasgupta, *ACS Energy Lett.* **2017**, *2*, 664.

[46] J. Park, J. Jeong, Y. Lee, M. Oh, M.-H. Ryou, Y. M. Lee, *Adv. Mater. Interfaces* **2016**, *3*, 1600140.

[47] M.-H. Ryou, Y. M. Lee, Y. Lee, M. Winter, P. Bieker, *Adv. Funct. Mater.* **2015**, *25*, 834.

[48] J. Ahn, J. Park, J. Y. Kim, S. Yoon, Y. M. Lee, S. Hong, Y.-G. Lee, C. Phatak, K. Y. Cho, *ACS Appl. Energy Mater.* **2019**, *2*, 5656.

[49] J. Heine, S. Krueger, C. Hartnig, U. Wietelmann, M. Winter, P. Bieker, *Adv. Energy Mater.* **2014**, *4*, 1300815.

[50] J. S. Kim, B. Sh, W. Y. Yoonz, *J. Electrochem. Soc.* **2010**, *157*, A984.

[51] A. Storelli, S. Rousselot, N. Alzate-Carvajal, V. Pelé, M. Dollé, *J. Electrochem. Soc.* **2021**, *168*, 040505.

**ADVANCED
SCIENCE NEWS**

www.advancedsciencenews.com

**ADVANCED
FUNCTIONAL
MATERIALS**

www.afm-journal.de

[52] D. Aurbach, Y. Gofer, *J. Electrochem. Soc.* **1989**, *136*, 3198.

[53] Y. Gu, W.-W. Wang, J.-W. He, S. Tang, H.-Y. Xu, J.-W. Yan, Q.-H. Wu, X.-B. Lian, M.-S. Zheng, Q.-F. Dong, B.-W. Mao, *ChemElectroChem* **2019**, *6*, 181.

[54] B. Yan, Y. Wang, H. Ren, X. Lu, M. Kotobuki, B. Liu, K. Jiang, *Int. J. Electrochem. Sci.* **2022**, *17*, 220513.

[55] R. Xu, F. Liu, Y. Ye, H. Chen, R. R. Yang, Y. Ma, W. Huang, J. Wan, Y. Cui, *Adv. Mater.* **2021**, *33*, 2104009.

[56] J. Kriegler, E. Jaimez-Farnham, M. Scheller, E. Dashjav, F. Konwitschny, L. Wach, L. Hille, F. Tietz, M. F. Zaeh, *Energy Storage Mater.* **2023**, *57*, 607.

[57] J. Kriegler, L. Hille, A. Oehler, M. Chaja, M. F. Zaeh, *J. Manuf. Processes* **2023**, *106*, 188.

[58] J. Kriegler, M. Finsterbusch, Y. Liang, E. Jaimez-Farnham, M. F. Zaeh, *J. Power Sources* **2024**, *596*, 234091.

[59] J. Kriegler, L. Hille, S. Stock, L. Kraft, J. Hagemeister, J. B. Habedank, A. Jossen, M. F. Zaeh, *Appl. Energy* **2021**, *303*, 117693.

[60] K.-H. Chen, M. J. Namkoong, V. Goel, C. Yang, S. Kazemiabnavi, S. M. Mortuza, E. Kazyak, J. Mazumder, K. Thornton, J. Sakamoto, N. P. Dasgupta, *J. Power Sources* **2020**, *471*, 228475.

[61] L. Hille, H.-C. Toepper, C. Schriever, J. Kriegler, J. Keilhofer, M. P. Noecker, M. F. Zaeh, *J. Electrochem. Soc.* **2022**, *169*, 060518.

[62] A. Sassmannshausen, A. Brenner, J. Finger, *J. Mater. Process. Technol.* **2021**, *293*, 117058.

[63] A. Temmler, D. Liu, J. Luo, R. Poprawe, *Appl. Surf. Sci.* **2020**, *510*, 145272.

[64] B. Zhang, H. Yang, H. Liu, J. Hao, X. Liu, *Appl. Surf. Sci.* **2022**, *573*, 151557.

[65] V. Furlan, A. G. Demir, B. Previtali, *Opt. Laser Technol.* **2015**, *75*, 164.

[66] G. C. de Giorgi, V. Furlan, A. G. Demir, E. Tallarita, G. Candiani, B. Previtali, *Proc. CIRP* **2016**, *49*, 88.

[67] G. C. de Giorgi, V. Furlan, A. G. Demir, E. Tallarita, G. Candiani, B. Previtali, *Appl. Surf. Sci.* **2017**, *406*, 199.

[68] A. G. Demir, V. Furlan, N. Lecis, B. Previtali, *Biointerphases* **2014**, *9*, 29009.

[69] G. Zhu, Z. Xu, Y. Jin, X. Chen, L. Yang, J. Xu, D. Shan, Y. Chen, B. Guo, *Opt. Lasers Eng.* **2022**, *157*, 107130.

[70] Y. K. Madhukar, S. Mullick, D. K. Shukla, S. Kumar, A. K. Nath, *Appl. Surf. Sci.* **2013**, *264*, 892.

[71] A. V. Rode, D. Freeman, K. G. H. Baldwin, A. Wain, O. Uteza, P. Delaporte, *Appl. Phys. A* **2008**, *93*, 135.

[72] T. Shi, C. Wang, G. Mi, F. Yan, *J. Manuf. Processes* **2019**, *42*, 60.

[73] M. Mosbacher, V. Dobler, J. Boneberg, P. Leiderer, *Appl. Phys. A: Mater. Sci. Process.* **2000**, *70*, 669.

[74] Z. Wang, X. Zeng, W. Huang, *Surf. Coat. Technol.* **2003**, *166*, 10.

[75] L. Chen, Y. Su, J. Zhang, H. Zhang, B. Fan, G. Shao, M. Zhong, C.-A. Wang, *ACS Appl. Mater. Interfaces* **2021**, *13*, 37082.

[76] N. Khosla, J. Narayan, R. Narayan, X.-G. Sun, M. P. Paranthaman, *J. Electrochem. Soc.* **2023**, *170*, 030520.

[77] M. Bolsinger, M. Weller, S. Ruck, P. Kaya, H. Riegel, V. Knoblauch, *Electrochim. Acta* **2019**, *330*, 135163.

[78] S. Afyon, F. Krumeich, J. L. M. Rupp, *J. Mater. Chem. A* **2015**, *3*, 18636.

[79] R. Murugan, V. Thangadurai, W. Weppner, *Angew. Chem., Int. Ed.* **2007**, *46*, 7778.

[80] M. Finsterbusch, T. Danner, C.-L. Tsai, S. Uhlenbruck, A. Latz, O. Guillon, *ACS Appl. Mater. Interfaces* **2018**, *10*, 22329.

[81] Z. D. Hood, Y. Zhu, L. J. Miara, W. S. Chang, P. Simons, J. L. M. Rupp, *Energy Environ. Sci.* **2022**, *15*, 2927.

[82] C. Sedlmeier, T. Kutsch, R. Schuster, L. Hartmann, R. Bublitz, M. Tominac, M. Bohn, H. A. Gasteiger, *J. Electrochem. Soc.* **2022**, *169*, 070508.

[83] J. Kasemchainan, S. Zekoll, D. Spencer Jolly, Z. Ning, G. O. Hartley, J. Marrow, P. G. Bruce, *Nat. Mater.* **2019**, *18*, 1105.

[84] Y. Kato, S. Hori, T. Saito, K. Suzuki, M. Hirayama, A. Mitsui, M. Yonemura, H. Iba, R. Kanno, *Nat. Energy* **2016**, *1*, 652.

[85] S. Randau, D. A. Weber, O. Koetz, R. Koerver, P. Braun, A. Weber, E. Ivers-Tiffée, T. Adermann, J. Kulisch, W. G. Zeier, F. H. Richter, J. Janek, *Nat. Energy* **2020**, *3*, 267.

[86] M. V. Reddy, C. M. Julien, A. Mauger, K. Zaghib, *Nanomaterials* **2020**, *10*, 1606.

[87] B. Stumper, A. Mayr, K. Mosler, J. Kriegler, R. Daub, *J. Electrochem. Soc.* **2023**, *170*, 060518.

[88] J. M. Liu, *Opt. Lett.* **1982**, *7*, 196.

[89] DIN Deutsches Institut für Normung e.V. Geometrical product specifications (GPS): Surface texture: Areal – Part 2: Terms, definitions and surface texture parameters (DIN EN ISO 25178-22:2019), Beuth Verlag GmbH, Berlin **2020**. [February 11, 2023].

[90] M. Murbach, B. Gerwe, N. Dawson-Elli, L. Tsui, *J. Open Source Software* **2020**, *5*, 2349.

[91] Y. Jee, M. F. Becker, R. M. Walser, *J. Opt. Soc. Am. B* **1988**, *5*, 648.

[92] J. Kriegler, T. M. Duy Nguyen, L. Tomcic, L. Hille, S. Grabmann, E. I. Jaimez-Farnham, M. F. Zaeh, *Results Mater.* **2022**, *15*, 100305.

[93] N. Hodgson, S. Heminga, A. Steinkopff, H. Haloui, T. S. Lee, presented at Proc. Lasers in Manufacturing Conf., Munich, Germany, June **2019**.

[94] B. N. Chichkov, C. Momma, S. Nolte, F. von Alvensleben, T. A. Femtosecond, *Appl. Phys. A* **1996**, *63*, 109.

[95] C. Momma, B. N. Chichkov, S. Nolte, F. von Alvensleben, A. Tünnermann, H. Welling, B. Wellegehausen, *Opt. Commun.* **1996**, *129*, 134.

[96] A. Spiro, M. Lowe, G. Pasmanik, *Appl. Phys. A* **2012**, *107*, 801.

[97] F. Siegel, U. Klug, R. Kling, *J. Laser Micro/Nanoeng.* **2009**, *4*, 104.

[98] J. Winter, M. Spellauge, J. Hermann, C. Eulenkamp, H. P. Huber, M. Schmidt, *Opt. Express* **2021**, *29*, 14561.

[99] H. Mustafa, R. Pohl, T. C. Bor, B. Pathiraj, D. T. A. Matthews, G. R. B. E Roemer, *Opt. Express* **2018**, *26*, 18664.

[100] P. Lickschat, D. Metzner, S. Weißmantel, *Int. J. Adv. Manuf. Technol.* **2020**, *109*, 1167.

[101] J. Cheng, W. Perrie, M. Sharp, S. P. Edwardson, N. G. Semaltianos, G. Dearden, K. G. Watkins, *Appl. Phys. A* **2009**, *95*, 739.

[102] M. C. Kong, J. Wang, *Proc. CIRP* **2014**, *13*, 417.

[103] G. Raciukaitis, M. Brikas, P. Gecys, M. Gedvilas, in *Accumulation Effects in Laser Ablation of Metals with High-Repetition-Rate Lasers* (Ed: C.R. Phipps), SPIE, Bellingham, USA **2008**, p.70052L, https://doi.org/10.1117/12.782937.

[104] K. T. Ahmmed, E. J. Y. Ling, P. Servio, A.-M. Kietzig, *Opt. Lasers Eng.* **2015**, *66*, 258.

[105] T. Jansen, D. Blass, S. Hartwig, K. Dilger, *Batteries* **2018**, *4*, 1.

[106] Y.-D. Chen, W.-J. Tsai, S.-H. Liu, J.-B. Horng, *Opt. Laser Technol.* **2018**, *107*, 180.

[107] A. Seo, A. Meyer, S. Shrestha, M. Wang, X. Xiao, Y.-T. Cheng, *Appl. Phys. Lett.* **2022**, *120*, 211602.

[108] C. A. Hart, C. H. Skinner, A. M. Capece, B. E. Koel, *J. Nucl. Mater.* **2016**, *468*, 71.

[109] Y. Li, Y. Li, Y. Sun, B. Butz, K. Yan, A. L. Koh, J. Zhao, A. Pei, Y.i Cui, *Nano Lett.* **2017**, *17*, 5171.

[110] C. Ma, Y. Cheng, K. Yin, J. Luo, A. Sharafi, J. Sakamoto, J. Li, K. L. More, N. J. Dudney, M. Chi, *Nano Lett.* **2016**, *16*, 7030.

[111] A. Sharafi, E. Kazyak, A. L. Davis, S. Yu, T. Thompson, D. J. Siegel, N. P. Dasgupta, J. Sakamoto, *Chem. Mater.* **2017**, *29*, 7961.

[112] S. Wenzel, S. J. Sedlmaier, C. Dietrich, W. G. Zeier, J. Janek, *Solid State Ionics* **2018**, *318*, 102.

[113] T. Krauskopf, H. Hartmann, W. G. Zeier, J. Janek, *ACS Appl. Mater. Interfaces* **2019**, *11*, 14463.

[114] T. Krauskopf, R. Dippel, H. Hartmann, K. Peppler, F. Mogwitz, F. H. Richter, W. G. Zeier, J. Janek, *Joule* **2019**, *3*, 2030.

**ADVANCED
SCIENCE NEWS**

www.advancedsciencenews.com

**ADVANCED
FUNCTIONAL
MATERIALS**

www.afm-journal.de

[115] A. Sharafi, H. M. Meyer, J. Nanda, J. Wolfenstine, J. Sakamoto, *J. Power Sources* **2016**, *302*, 135.

[116] M. Liu, M. Zhang, S. Liu, H. Chen, B. Li, G. Li, S. Zhang, Y. Wen, J. Qiu, J. Chen, P. Zhao, *J. Power Sources* **2024**, *593*, 233977.

[117] K. J. Kim, J. L. M. Rupp, *Energy Environ. Sci.* **2020**, *13*, 4930.

[118] J. van den Broek, S. Afyon, J. L. M. Rupp, *Adv. Energy Mater.* **2016**, *6*, 1600736.

[119] R. Pfenninger, S. Afyon, I. Garbayo, M. Struzik, J. L. M. Rupp, *Adv. Funct. Mater.* **2018**, *28*, 1800879.

[120] J. van den Broek, J. L. M. Rupp, S. Afyon, *J. Electroceram.* **2017**, *38*, 182.

[121] C. Zou, L. Yang, K. Luo, L. Liu, X. Tao, L. Yi, X. Liu, X. Zhang, X. Wang, *ACS Appl. Energy Mater.* **2022**, *5*, 8428.

[122] F. Duffner, N. Kronemeyer, J. Tuebke, J. Leker, M. Winter, R. Schmuch, *Nat. Energy* **2021**, *6*, 123.

[123] J. Schnell, T. Günther, T. Knoche, C. Vieider, L. Köhler, A. Just, M. Keller, S. Passerini, G. Reinhart, *J. Power Sources* **2018**, *382*, 160.

[124] K. van der Straeten, O. Nottrodt, M. Zuric, A. Olowinsky, P. Abels, A. Gillner, *Proc. CIRP* **2018**, *74*, 491.

[125] U. Loeschner, J. Schille, A. Streek, T. Knebel, L. Hartwig, R. Hillmann, C. Endisch, *J. Laser Appl.* **2015**, *27*, S293031.

[126] L. Hille, J. Kriegler, A. Oehler, M. Chaja, S. Wagner, M. F. Zaeh, *J. Laser Appl.* **2023**, *35*, 042054.

[127] D. Brinkmeier, D. Holder, A. Loescher, C. Röcker, D. J. Förster, V. Onuseit, R. Weber, M. Abdou Ahmed, T. Graf, *Appl. Phys. A* **2022**, *128*, 35.